J. Fluid Mech. (1998), *vol.* 373, *pp.* 193–219. Printed in the United Kingdom

Modelling of concentrated suspensions using a continuum constitutive equation

By SAMUEL R. SUBIA[1]†, MARC S. INGBER[1], LISA A. MONDY[2], STEVE A. ALTOBELLI[3]‡, AND ALAN L. GRAHAM[4]

[1]Department of Mechanical Engineering, University of New Mexico, Albuquerque, NM 87131, USA

[2]Energetic and Multiphase Processes Department, Sandia National Laboratories, Albuquerque, NM 87185, USA

[3]The Lovelace Institutes, 2345 Ridgecrest Drive SE, Albuquerque, NM 87108, USA

[4]Los Alamos National Laboratory, ESA-EPE, Los Alamos, NM 87545, USA

(Received 4 November 1996 and in revised form 18 May 1998)

We simulate the behaviour of suspensions of large-particle, non-Brownian, neutrally-buoyant spheres in a Newtonian liquid with a Galerkin, finite element, Navier–Stokes solver into which is incorporated a continuum constitutive relationship described by Phillips *et al.* (1992). This constitutive description couples a Newtonian stress/shear-rate relationship (where the local viscosity of the suspension is dependent on the local volume fraction of solids) with a shear-induced migration model of the suspended particles. The two-dimensional and three-dimensional (axisymmetric) model is benchmarked with a variety of single-phase and two-phase analytic solutions and experimental results. We describe new experimental results using nuclear magnetic resonance imaging to determine non-invasively the evolution of the solids-concentration profiles of initially well-mixed suspensions as they separate when subjected to slow flow between counter-rotating eccentric cylinders and to piston-driven flow in a pipe. We show good qualitative and quantitative agreement of the numerical predictions and the experimental measurements. These flows result in complex final distributions of the solids, causing rheological behaviour that cannot be accurately described with typical single-phase constitutive equations.

1. Introduction

Particle-laden shear flows are important in a wide variety of applications including hydraulic fracturing technology (Clifton, Brown & Wang 1988; Unwin & Hammond 1990; Baree & Conway 1994), processing of solid-rocket propellants (Husband 1989), ceramics and reinforced polymer composites (Givler, Crochet & Pipes 1983), and the transport of slurries (Leighton & Acrivos 1986). Successful use of suspensions in engineering processes often requires that a flowing suspension be supplied at a specified location with a prescribed particle concentration. In the past, applications involving suspensions drew heavily upon the experience of engineers to predict the

† Present address: Energetic and Multiphase Processes Department, Sandia National Laboratories, Albuquerque, NM 87185, USA.

‡ Present address: New Mexico Resonance, 2425 Ridgecrest Drive SE, Albuquerque, NM 87108, USA.

flow behaviour and the evolution of the particle concentration profile. As applications grow increasingly complex, design specifications become more critical and adjustments must be made if the specifications are to be met. Ultimately, the behaviour of the flowing suspension must be better understood in order to effectively control particle concentrations throughout an application process.

It has long been recognized that flowing suspensions exhibit gross particle movement, that is, the particles "migrate" within the flow (Karnis, Goldsmith & Mason 1966; Arp & Mason 1977; Leighton & Acrivos 1987*a*; Abbott *et al.* 1991). Here we are considering only large Péclet number systems, where classical diffusion is neglible. In examining these systems Leighton & Acrivos (1987*b*) proposed scaling arguments which identified three causes of particle migration and diffusion, namely shear-rate gradients, relative viscosity gradients and concentration gradients. For succinctness we will henceforth refer to particle migration due to shear-rate gradients and particle motion due to viscosity or concentration gradients as shear-induced migration.

In order to better understand this shear-induced migration, numerical simulations of particles suspended in liquid flows have been carried out using several methods. One approach is to simulate the individual motions of particles with Stokesian dynamics (Brady & Bossis 1988). Other methods that explicitly include the effects of suspended particles employ boundary element formulations (Ingber 1989; Tran-Cong & Phan-Thien 1989; Karilla, Fuentes & Kim 1989). Although the present generation of computers has made this approach a more viable one, it is still somewhat limited in terms of the problem size which be solved.

Another approach is to model the suspension as an effective continuum. Suspension balance models (Jenkins & McTigue 1990; Nott & Brady 1994) provide a non-local description of suspension behaviour in terms of the particle's velocity fluctuations. Nott & Brady showed that a constant suspension pressure normal to the direction of mean flow motion leads to particle migration and concentration variations in inhomogenous flow. In yet another somewhat simpler approach (referred to herein as the diffusive flux model), the suspension is modelled as a single continuum whereby the scaling arguments of Leighton & Acrivos (1987*b*) are used to form the basis of a nonlinear constitutive model for the particle concentration in a flowing suspension (Phillips *et al.* 1992).

Within the context of the single-continuum model, an important consequence of particle migration is that the momentum equation for the suspension flow becomes nonlinear, since the effective viscosity of the suspension varies with particle concentration. Phillips *et al.* (1992) used the finite difference method to study shear-induced particle migration in wide-gap Couette devices. Similar modelling studies of Couette devices have been performed by Fang & Phan-Thien (1995), and Phan-Thien *et al.* (1995) with the finite volume method. Zhang & Acrivos (1994) used the finite element method to examine shear-induced migration coupled with viscous resuspension in pipe flows.

Phillips *et al.* (1992) point out a shortcoming of the single-continuum model in that the particle concentration assumes the maximum packing value in regions of flow where the shear rate is zero valued. The model is also known to predict particle migration in a parallel-plate viscometer where no net migration of particles is observed experimentally (Chapman 1990; Chow *et al.* 1994). Krishnan, Beimfohr & Leighton (1996) suggest modifications to the original model of Phillips *et al.* which include the effects of curvature to resolve the discrepancy noted in the parallel-plate viscometer.

For the case of steady-state suspension flow in a pipe geometry the model of Phillips *et al.* (1992) predicts a concentration profile with a cusp at the pipe centre.

Mills & Snabre (1995) present a model based upon lubrication forces between colliding particles that specializes to the model of Phillips *et al.* in the problems of Couette flow and pipe flow. In the pipe flow problem, Mills & Snabre suggest the use of a non-local stress tensor to overcome the presence of the centreline cusp in the concentration profile. However, this approach cannot be used in any other geometry, and furthermore, recent experiments of concentrated suspension pipe flows (Hampton *et al.* 1997) indicate that the particle concentrations do indeed become locally high along the centreline.

In this paper, we incorporate the diffusive flux model into a finite element method (FEM) formulation to model shear-induced particle migration in non-homogeneous shear flows of suspensions. The purpose of the work is to create an operational framework within which to consider new problems in fluid suspension flows, and to identify possible limitations within this framework. Since the finite element modelling methodology is fairly well established in the design community, it seemed appropriate to demonstrate that general fluid suspension problems can indeed be studied using the FEM. In conducting this study, we evaluate the methodology within a shared resource computing environment and not on dedicated compute servers, so that computational efficiency was not a primary consideration. With this purpose in mind, we began with an existing, two-dimensional, Navier–Stokes, finite element computer code NACHOS II (Gartling 1986), and modified the code in order to study some basic problems of shear-induced particle migration in suspension flows.

We limit our attention in this paper to suspending fluids containing neutrally buoyant particles. In the following sections, we describe the mathematical model and the finite element formulation. Then, in subsequent sections, we apply the current FEM formulation to several problems. First, we demonstrate the ability to apply the FEM methodolgy to a couple of problems where analytical solutions are known. Next we document some new experiments pertaining to suspension flows and attempt to provide some insight into the suspension behaviour. These experiments use nuclear magnetic resonance (NMR) imaging techniques to determine non-invasively the distribution of suspended solids as the initially well-mixed suspensions demix when subjected to flow conditions. Here the tested flows were designed to be two-dimensional. Finally, we compare our numerical simulation results to these experimental findings.

2. Mathematical formulation

We consider solid particles suspended by a Newtonian fluid. The distribution of these particles in the suspension has a direct influence upon the velocity field, and conversely, the velocity field has a direct influence on the movement of the particles. In the current study, we limit our attention to neutrally buoyant suspensions. Rather than explictly model both the particles and the fluid as distinct continuum phases, we instead model the two-phase suspension as a single continuum.

For neutrally-buoyant particles suspended in an incompressible fluid, the conservation of mass principle requires that the mass-averaged suspension velocity field be divergence free. That is

$$\frac{\partial u_i}{\partial x_i} = 0, \tag{2.1}$$

where u_i are the components of velocity.

The corresponding momentum equation is given by

$$\rho_o \left(\frac{\partial u_i}{\partial t} + u_j \frac{\partial u_i}{\partial x_j} \right) = \frac{\partial \tau_{ij}}{\partial x_j}, \tag{2.2}$$

where ρ_o is the suspension mass density, and τ_{ij} is the stress tensor.

As in Phillips *et al.*, here we assume that the constitutive equation for total stress τ_{ij} is given by the generalized Newtonian relationship

$$\tau_{ij} = -P + 2\mu(\phi) D_{ij}, \tag{2.3}$$

where P is the pressure, ϕ is the volume fraction of solids in the suspension, $\mu(\phi)$ is the effective suspension viscosity, and D_{ij} is the deformation rate tensor.

In treating the particle suspension as a single continuum one must account for variation in suspension viscosity with particle concentration. This variation in viscosity is obtained as a simple correction to the solvent viscosity so that the effective suspension viscosity $\mu = \mu_r \mu_s$, where μ_s is the solvent viscosity and μ_r is the relative viscosity of the suspension. Several researchers, most notably Krieger (1972) and Leighton & Acrivos (1987*b*), have proposed empirical correlations for the relative viscosity. We consider here the correlation of Krieger given by

$$\mu_r = \left(1 - \frac{\phi}{\phi_m} \right)^{-1.82}, \tag{2.4}$$

where ϕ_m is the maximum solid volume fraction for which the suspension exhibits fluid behaviour.

The value of ϕ_m depends upon the uniformity of particle size, the effective microstructure of the packed configuration and the type of flow. For uniform diameter particles the value of ϕ_m can vary over a range from $\phi_m = 0.52$ (simple cubic packing) to $\phi_m = 0.74$ (face-centred cubic packing). Still other values of ϕ_m are applicable to randomly packed particles and bimodal suspensions. In this research, we assume that $\phi_m = 0.68$ in all calculations, as in the high-shear limit value used by Krieger (1972); however ϕ_m could be considered an adjustable parameter.

In practical flow problems, the local particle concentration varies with time and must be known in order to evaluate the total stress. Here we introduce an evolution equation for particle volume fraction ϕ as

$$\frac{\partial \phi}{\partial t} + u_i \frac{\partial \phi}{\partial x_i} = -\frac{\partial N_i}{\partial x_i}. \tag{2.5}$$

This equation represents a balance between stored particles, the convected particle flux and diffusive particle flux, N. Note that the momentum and concentration equations are now tightly coupled, not only through the velocity field but also through the concentration-dependent relative viscosity.

Several mechanisms which include Brownian motion, sedimentation, hydrodynamic particle interactions, and gradients in suspension viscosity may contribute to the particle flux. Neglecting Brownian motion and assuming that sedimentation is not present due to neutral buoyancy of the particles, we model the diffusive particle flux as

$$N = N_\mu + N_c, \tag{2.6}$$

where N_μ is the flux contribution due to spatial variations in viscosity and N_c is the flux contribution due to hydrodynamic particle interactions. Based on the scaling

arguments of Leighton & Acrivos (1987*b*), Phillips *et al.* (1992) proposed

$$N_c = -a^2 \phi K_c \nabla(\dot{\gamma}\phi) \tag{2.7}$$

and

$$N_\mu = -a^2 \phi^2 \dot{\gamma} K_\mu \nabla(\ln \mu) \tag{2.8}$$

where a is the characteristic particle length (e.g. radius), $\dot{\gamma}$ is the local shear rate, and K_μ and K_c are empirically-determined coefficients. The particle flux considered here is driven not only by gradients of concentration, but also by gradients of the shear rate.

Equation (2.5) was employed by Phillips *et al.* (1992) to predict particle migration in unidirectional shear flows for which the flow can be characterized by the local shear rate. By direct analogy with one-dimensional flows, we employ a measure of the generalized shear rate $\dot{\gamma}$ as

$$\dot{\gamma} = (2D_{ij}D_{ij})^{1/2}. \tag{2.9}$$

3. Finite element formulation

We multiply each governing equation by a weighting function and integrate over the volume of the problem domain Ω to obtain a weighted residual statement. Performing an integration by parts on the momentum and concentration equations allows us to equally distribute integration between the weighting function and the solution variables. This enables us to obtain an alternative weak formulation (Zienkiewicz 1967) of the governing equations in which the continuity requirements of the solution variables are reduced.

We introduce nodal basis functions for velocity, pressure, and particle concentration to obtain the following representations:

$$u_i = \Phi^T u_i^e, \qquad P = \Psi^T P_i, \qquad \phi = \Phi^T \phi_i. \tag{3.1}$$

Selecting the weighting function for the momentum equation from the basis functions used in the approximation of u_i, and the weighting function for the particle volume fraction from the basis functions used in the approximation of ϕ, we obtain a standard Galerkin finite element formulation (Gartling & Reddy 1994). By requiring that the residuals be identically zero, we arrive at the following governing weak formulations for continuity, momentum, and particle concentration:

$$-\left[\int_\Omega \Psi \frac{\partial \Phi}{\partial x_i} \mathrm{d}\Omega\right] u_i^e = 0, \tag{3.2}$$

$$\left[\int_\Omega \rho_o \Phi \Phi^T \mathrm{d}\Omega\right] \dot{u}_i^e + \left[\int_\Omega \rho_o \Phi \Phi^T u_j^e \frac{\partial \Phi^T}{\partial x_j} \mathrm{d}\Omega\right] u_i^e + \left[\int_\Omega \mu \frac{\partial \Phi}{\partial x_j} \frac{\partial \Phi^T}{\partial x_j} \mathrm{d}\Omega\right] u_i^e + \left[\int_\Omega \mu \frac{\partial \Phi}{\partial x_j} \frac{\partial \Phi^T}{\partial x_i} \mathrm{d}\Omega\right] u_j^e - \left[\int_\Omega \frac{\partial \Phi}{\partial x_i} \Psi^T \mathrm{d}\Omega\right] P = \int_\Gamma \Phi^T \tau_{ij} n_j \mathrm{d}\Gamma, \tag{3.3}$$

$$\left[\int_\Omega \Phi \Phi^T \mathrm{d}\Omega\right] \dot{\phi} + \left[\int_\Omega \Phi \Phi^T u_j^e \frac{\partial \Phi^T}{\partial x_j} \mathrm{d}\Omega\right] \phi + \left[\int_\Omega \frac{\partial \Phi}{\partial x_j} a^2 \left\{K_c \left[\frac{\partial \dot{\gamma}}{\partial x_j} \Phi^T \phi \Phi^T + \dot{\gamma} \Phi^T \phi \frac{\partial \Phi^T}{\partial x_j}\right] + K_\mu \dot{\gamma} \Phi^T \phi \Phi^T \phi \frac{1}{\mu} \frac{\partial \mu}{\partial \phi} \frac{\partial \Phi^T}{\partial x_j}\right\} \mathrm{d}\Omega\right] \phi = \int_\Gamma \Phi^T N_j n_j \mathrm{d}\Gamma. \tag{3.4}$$

The above equations contain solution variables u, P, and ϕ which are functions of time. In these equations, both u and ϕ are assumed to be continuous over the problem domain. The equations also contain values of $\dot{\gamma}$ and μ which are functions of the solution variables themselves. In the present formulation we allow for explicit spatial and temporal variation of these values within an element as

$$u_i(x_i, t) = \Phi^T(x_i)\hat{u}_i^e(t), \qquad \phi(x_i, t) = \Phi^T(x_i)\hat{\phi}_i(t), \tag{3.5}$$

$$P(x_i, t) = \Psi^T(x_i)\hat{P}_i(t), \tag{3.6}$$

$$\mu(x_i, t) = \Psi^T(x_i)\hat{\mu}_i(t), \qquad \dot{\gamma}(x_i, t) = \Psi^T(x_i)\hat{\dot{\gamma}}(t), \tag{3.7}$$

where the hat quantities are arrays of the solution variables evaluated at the nodes. This formulation is able to directly accommodate boundary conditions of velocity, traction, and particle concentration. Additionally, it is also possible to include boundary conditions of apparent wall slip velocity such as suggested by Jana, Kapoor & Acrivos (1995). Although slip conditions may indeed be important, especially at high particle concentrations, these conditions were not employed in any of the simulations described herein.

Since particle migration depends upon the value of the generalized shear rate $\dot{\gamma}$, it is important that we be able to accurately compute this quantity without increasing the continuity requirements of u_i. Use of a biquadratic Lagrangian basis function for u_i allows a bilinear representation of $\dot{\gamma}$ within the element, but unfortunately $\dot{\gamma}$ is often discontinuous across elements. In our formulation we employ a technique often used to smooth primitive variables (Lee, Gresho & Sani 1979) by which one computes $\dot{\gamma}$ at element quadrature points and then extrapolates these values as averages to the nodal points. The present formulation also employs a biquadratic Lagrangian basis function for the particle concentration, thus the approximation for ϕ is continuous within the computational domain.

Our two-dimensional FEM formulation differs from the three-dimensional FEM formulation of Zhang & Acrivos (1994) in several respects. Whereas Zhang & Acrivos employ a penalty formulation for pressure, here we employ a mixed formulation in which pressure becomes a solution variable. The present formulation is implicit, as opposed to the explicit formulation of Zhang & Acrivos, so that all convective and diffusive terms are retained in the nonlinear and non-symmetric system matrix. Finally, the governing equations are solved as a single coupled system and not as segregated equations. In the following sections, we apply the current FEM formulation to several problems. Mesh refinement studies were performed for all numerical results presented to ensure the results were properly converged.

4. Numerical benchmark results

4.1. *Concentric Couette*

Noting that the shear rate in a wide-gap concentric Couette device varied radially across the wide gap, Abbott *et al.* (1991) used the device to observe the shear-induced particle migration of a suspension as the particle concentration evolved from an initially uniform profile to the non-uniform steady-state profile. In these experiments, the outer cylinder of radius R_o was held stationary while the inner cylinder of radius R_i was rotated at a constant angular velocity. NMR images of the Couette device taken during the development to steady state provided a means by which to determine the extent of shear-induced particle migration in the Couette gap for various particle sizes

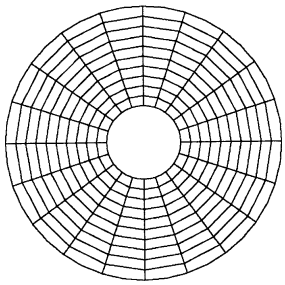

FIGURE 1. FEM discretization for the concentric Couette problem.

and different initial concentrations. From these experiments, Abbott *et al.* determined that the particle migration for unimodal suspensions depended upon the total strain and not upon the strain rate.

For the radial geometry of the Couette device, Phillips *et al.* used (2.2), (2.5), (2.6), and the Krieger model of suspension viscosity (2.4) to determine an analytic expression for the steady-state particle volume fraction ϕ as

$$\frac{\phi}{\phi_w} = \left(\frac{r}{R_i}\right)^2 \left(\frac{1-\phi_w/\phi_m}{1-\phi/\phi_m}\right)^{1.82(1-K_\mu/K_c)}, \tag{4.1}$$

where ϕ_w is the value of ϕ at the inner cylinder and the ratio K_c/K_μ was experimentally determined. Under the assumptions of their analysis, the steady-state particle distribution was found to be independent of particle size.

The above expression which is transcendental in ϕ must be solved in conjunction with the momentum relation and the physical constraint stating that the average particle volume fraction

$$\bar{\phi} = \frac{2}{R_o^2 - R_i^2} \int_{R_i}^{R_o} \phi r \, \mathrm{d}r \tag{4.2}$$

must remain unchanged in the closed system bounded by the inner and the outer cylinder.

Phillips *et al.* (1992) performed numerical simulations of the transient experiments of Abbott *et al.* (1991) using a one-dimensional finite difference method. Since the concentration depends upon the total strain, they expressed their results in terms of the number of rotations of the inner cylinder. Through a combined analysis of the experimental data and the numerical simulation results, they determined optimal values for their model parameters of $K_c = 0.41$ and $K_\mu = 0.62$ ($K_c/K_\mu = 0.66$) for an initial uniform particle volume fraction of $\bar{\phi} = 0.55$, with 678 μm spherical particles.

The concentric Couette problem has also been numerically modelled two-dimensionally using a finite volume method. Fang & Phan-Thien (1995) have analysed the problem on a structured grid and Phan-Thien *et al.* (1995) did likewise on an unstructured grid. These finite volume analyses were pseudo-transient calculations containing roughly 4000 unknowns and both of these analyses produced good agreement with the steady-state analytic result. As a benchmark test of the present FEM formulation, we too set out to model the Couette experiments (Abbott *et al.* 1991; Phillips *et al.* 1992) for a concentrated suspension.

In applying the FEM to the concentric Couette problem, the device was spatially discretized using 240 quadrilateral finite elements as shown in figure 1. The FEM formulation includes four degrees of freedom per node, two velocity components,

pressure, and the particle volume fraction. Thus, the discretization results in 2740 unknowns. Using this discretization, a transient analysis was then performed with the NACHOS II code to determine the time evolution of particle concentration in the Couette device. In this simulation, the empirical constants were taken to be $K_c = 0.41$ and $K_\mu = 0.62$ as discussed above. The analysis was carried out for an initial particle volume fraction ϕ_o of 0.55 to a time corresponding to 800 turns of the inner cylinder. The results of this analysis are summarized in figure 2, which includes comparisons of the computed particle volume fraction across the Couette gap with the steady-state analytic solution and the steady-state experimental data, as well as a similar comparison with the experimental results for 100 turns.

Prior to the completion of 100 turns, the computed concentration profile in the Couette gap contains a region where the concentration decreases with increasing radius. This behaviour was observed experimentally by Phillips *et al.* (1992) and appears contrary to the premise of their model, since the shear rate in the gap decreases in the radial direction. However, the model does in fact predict this non-monotonicity during the development of the concentration profile. Particles near the inner cylinder experience both a higher shear rate and shear rate gradient than the particles situated further away from the inner cylinder. Thus the particle flux (2.6) is higher near the inner cylinder, and with regard to shear-induced migration in an initially uniform concentration, particles near the inner cylinder are in a sense impeded by particles further from the cylinder. For fewer than 100 rotations of the inner cylinder, this effect leads to a local decrease in the particle volume fraction in the gap with increasing radial coordinate. As the suspension is further strained, this localized behaviour is smoothed by concentration gradients and eventually the concentration becomes strictly increasing with radial coordinate.

The FEM results are shown to be in good agreement with the experimental results over the central portion of the gap region. The largest discrepancies between experimental and FEM results occur near the inner cylinder where the numerical results show a lower concentration than the experimental profiles. It is possible that a concentration-dependent ratio of K_c/K_μ could alleviate these discrepancies as it has been conjectured (Mondy *et al.* 1994; Tetlow *et al.* 1998) that the relative importance of collision- versus viscosity-induced particle motion diminishes with decreasing concentration. A comparison between the analytic solution, the FEM results (800 turns) and the experiment (12 000 turns) may imply the presence of localized wall effects which have been observed in other experiments (Hampton *et al.* 1997; Tetlow *et al.* 1998), but are not accounted for in the present single-continuum model.

4.2. *Pipe flow*

We consider here pressure-driven axial flow of a suspension through a pipe. Phillips *et al.* (1992) previously derived an analytical expression for the steady-state particle concentration for this problem in a pipe of outer radius R_o. Employing the Krieger model of suspension viscosity, they first solved for the shear rate in the pipe, and noted that the shear rate was largest at the pipe wall and decreased with radius before vanishing at the pipe centreline. Using this shear rate, they were then able to derive an expression for the steady-state particle concentration

$$\frac{\phi}{\phi_w} = \frac{R_o}{r}\left(\frac{1-\phi_w/\phi_m}{1-\phi/\phi_m}\right)^{1.82(1-K_\eta/K_c)}, \tag{4.3}$$

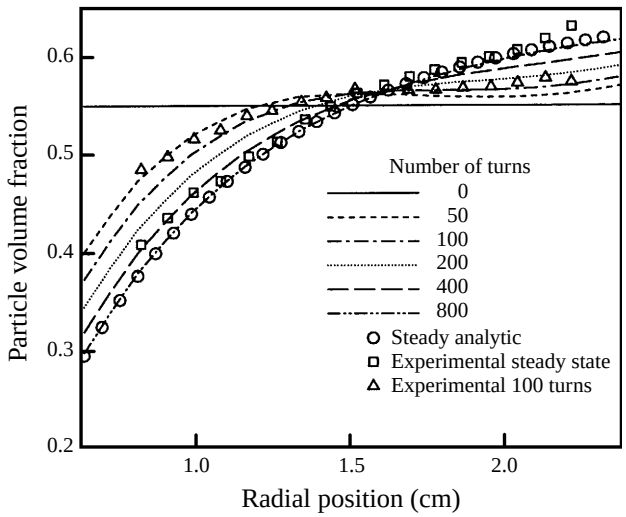

FIGURE 2. Particle distribution in the concentric Couette device for $\phi_o = 0.55$.

where ϕ_w is the particle volume fraction at the pipe wall. The value of ϕ_w was determined by assuming that the average particle volume fraction must remain unchanged so that

$$\bar{\phi} = \frac{2}{A}\int_0^{R_0} \phi r \, \mathrm{d}r, \tag{4.4}$$

where A is the cross-sectional area perpendicular to the flow direction. Since the shear rate decreases with radius, the Phillips solution for pipe flow predicts that the suspension particles will migrate toward the pipe centreline where the particle concentration reaches a value $\phi = \phi_m$. Thus the model predicts a distribution of particles which includes a cusp in particle concentration at the pipe centre, a result which has been questioned (Nott & Brady 1994; Koh, Hookham & Leal 1994). Recent experimental evidence (Hampton *et al.* 1997) indicates that a spike in the particle concentration actually does occur along the pipe axis, but the particle concentration at the pipe centre remains slightly less than ϕ_m for moderate to concentrated suspensions, $0.20 \leqslant \bar{\phi} \leqslant 0.50$.

Strictly speaking, the constraint (4.4) used by Phillips applies to a system of fixed mass and is invalid for an open flow system. Since the suspension flows through the pipe, the constraint should instead be based upon average suspension mass flux $\overline{\rho_s v}$ rather than area-averaged particle concentration. Employing a volume-fraction-weighted suspension density, alternative constraint relations can be written for the neutrally-buoyant suspension in terms of either particle mass flux or the suspension fluid mass flux. Here we consider a developing pipe flow in which the flow far upstream has a constant initial particle concentration. Under this condition, the input flux of particles with mass density ρ_p is $\rho_p\overline{\phi v} = \rho_p\bar{\phi}\bar{v}$, where $\bar{v}$ is the mean velocity at the pipe inlet and can be determined based upon the initial flow rate. Then for steady developed flow far downstream of the inlet, the constraint relation becomes

$$\bar{\phi} = \frac{2}{A\bar{v}}\int_0^{R_o} \phi v r \, \mathrm{d}r. \tag{4.5}$$

Thus the steady-state particle concentration is still given by (4.3), but the value of ϕ_w is now determined using the above constraint equation.

Since duct flows are quite common in the manufacture of products which utilize particle suspensions, it is important that our formulation be capable of analysing these problems. In a Newtonian fluid flow, the velocity field would become fully developed within several pipe diameters downstream from the inlet, but in the presence of suspended particles, the coupled velocity and concentration profiles develop much more slowly. From the previous work of Nott & Brady (1994), we note that the steady-state concentration profile prevails only at a fairly long development length ratio, L/R_o, which is roughly estimated to be on the order of

$$\frac{L}{R_o} \sim \left(\frac{R_o}{a}\right)^2 \tag{4.6}$$

for concentrated suspensions ($\bar{\phi} > 0.3$) where L is the particle concentration development length, R_o is the pipe radius, and a is the particle radius. As an example, for a 2.54 cm radius pipe and suspension particles of 3175 μm diameter then $L/R_o \sim 64$.

Recent experiments indicate that this development length ratio may be from one-third to one-half of that predicted by (4.6) (Hampton 1996). Similar results were also obtained in the numerical simulations of Phan-Thien & Fang (1996). Determining these fully developed velocity and concentration profiles numerically is most efficiently accomplished with codes similar to that of Zhang & Acrivos (1994) in which one effectively marches down the pipe analysing individual sections. The alternative, and more computationally expensive approach is to analyse the entire flow domain by modelling a single long section of pipe. Rather than model a very long section of pipe, we decided to model only a smaller section of the pipe and simulate the transient evolution of a startup flow as it evolves to a steady state.

A spatial discretization of a 122 cm long pipe with radius 2.54 cm ($L/R_o = 48$) was obtained using 245 axisymmetric elements resulting in 3483 degrees of freedom. Boundary conditions on particle volume fraction include a constant value of 0.50 volume fraction maintained at the inlet and zero diffusive flux ($N = 0$) conditions on particle concentration at the centreline, outer wall, and pipe exit. Zero velocity boundary conditions are imposed at the pipe wall and a zero normal stress is specified at the pipe exit. The zero normal stress condition at the exit serves only to specify a datum for the normal stress level, since it is the difference in stress between the inlet and outlet which drives the flow. We assume that from rest, a uniformly mixed suspension of 3178 μm diameter spherical particles with initial particle volume fraction $\phi_o = 0.50$ is suddenly subjected to a parabolic velocity profile at the pipe inlet.

Although the inlet velocity condition used in our numerical simulation is unrealistic, it allows development of the concentration and velocity profiles in a much shorter length of pipe. At early times in the simulation the velocity field includes radial flow components near the pipe inlet. However, our primary interest here lies in the fully developed exiting flow which is parallel to the pipe centreline axis even at early times. We show the computed particle volume fraction at the pipe exit in figure 3 where the numerical results are compared to the analytic steady-state solution of Phillips *et al.* (1992). As expected, the computed exit concentrations are somewhat less uniform than the analytic steady-state solution. The scaled velocity profiles, u/u_{max}, for the steady analytic solution, the imposed inlet parabolic profile, and the numerical FEM solution at the pipe exit are shown in figure 4. The FEM result is blunted when compared to the parabolic profile and is very similar in shape to that of the steady-state result. While we have not analysed the pipe flow to its fully developed state, we do expect in many applications that details of the developing flow and the

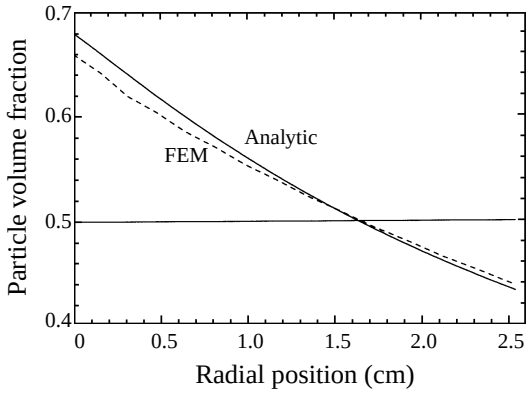

FIGURE 3. Pipe flow particle volume fraction distribution at exit for $\phi_o = 0.50$.

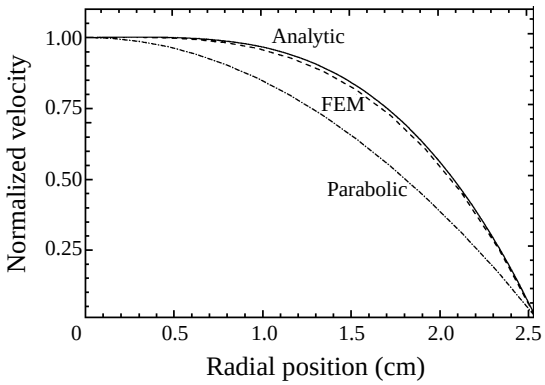

FIGURE 4. Pipe flow normalized velocity distribution at exit for $\phi_o = 0.50$.

development length will be important. This type of FEM anaylsis can be useful for these applications.

4.3. *Eccentric bearing simulations for a Newtonian liquid*

Steady flows in both the concentric Couette device and the pipe are two-dimensional flows which are unidirectional in nature. We now consider a benchmark problem which cannot be reduced to a one-dimensional problem, the lubrication problem for an eccentric bearing. This problem, which is shown schematically in figure 5, is similar to the concentric Couette problem except that now the inner cylinder is offset from the centre of the outer cylinder by some distance e. The eccentricity ratio is defined as $\varepsilon = e/(R_o - R_i)$. In this paper, we limit our attention to the case of a rotating inner cylinder and a stationary outer cylinder. This particular flow problem has been studied extensively in the fluid mechanics literature, both analytically and numerically.

Wannier (1950) assumed that for low Reynolds numbers the influence of fluid inertia was neglible in the eccentric bearing. By employing a transformation to bipolar coordinates along with a stream function approach, he was able to obtain an analytical solution to the corresponding Newtonian fluid problem for Stokes flow. An initial attempt by Kamal (1966) to study the effects of inertia by determining a linearized perturbation solution for the Stokes flow problem of the eccentric bearing proved less than successful, but nevertheless led the way for the improved and the

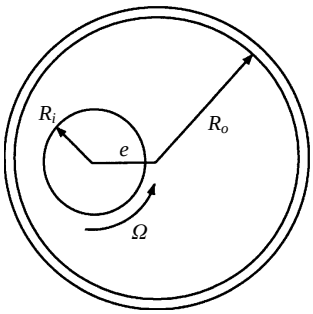

FIGURE 5. Eccentric bearing geometry.

more complete first-order perturbation solutions of Ballal & Rivlin (1976). In these solutions, it was shown that below some critical value of eccentricity, the primary circumferential fluid flow is directed upon pathlines which resemble those of the concentric Couette device but shifted toward the direction of inner cylinder offset. For a given problem geometry, analytical solutions of DiPrima & Stuart (1972) and of Ballal & Rivlin predict that beyond some critical value of eccentricity, the flow will separate in the wide-gap region. This separated flow sets up a region of slow recirculation in which the magnitude of flow velocities is roughly 1/100 of that in the circumferential flow. Ballal & Rivlin were also able to predict the position for the centre of the separated recirculating flow and stated that for increasing inertial effects this centre would move in the direction of the primary flow about the rotating cylinder.

The eccentric bearing Newtonian fluid lubrication problem has also been studied numerically by a variety of methods. Sood & Elrod (1970) used a finite difference method to solve the problem using the nonlinear Navier–Stokes equation. The Stokes flow eccentric bearing problem was solved by Kelmanson (1984) who employed a velocity stream function formulation and the boundary integral method. Using the velocity stream function in a Galerkin formulation with B-spline basis functions, San Andres & Szeri (1984) studied the eccentric bearing problem and were able to solve the Navier–Stokes equation up to Reynolds number ($Re = R_i^2 \Omega \rho / \mu$) of 80. All the numerical solutions cited here provide general agreement with the analytical solutions of Ballal & Rivlin (1976).

Before proceeding with the analysis of suspension flows, it is appropriate to first perform a qualitative test of the NACHOS II code by analysing the eccentric bearing problem for a Newtonian fluid. Two independent problems were analysed at $Re = 0.09$, one for an eccentricity ratio $\varepsilon = \frac{1}{3}$ and another for $\varepsilon = \frac{1}{2}$. These ratios were chosen in order to demonstrate the two types of eccentric bearing flow behaviour, with and without separation, which can be easily distinguished by the presence of a recirculation zone in the separated flow case. The FEM grids used in these analyses are shown in figure 6. Fluid flow pathlines from these respective analyses shown in figure 7 clearly indicate the two types of flow and provide confirmation that the fluid mechanics portion of the code has remained operational. For $\varepsilon = \frac{1}{2}$ two additional cases at $Re = 5$ and $Re = 10$ were considered. Figure 8 demonstrates that one of the effects of inertia is to move the centre of rotation for the recirculating flow in the direction of inner cylinder motion, and is again consistent with the predictions of Ballal & Rivlin (1976). Having performed some preliminary checks of the FEM code, we now proceed to study the eccentric bearing problem for a suspension.

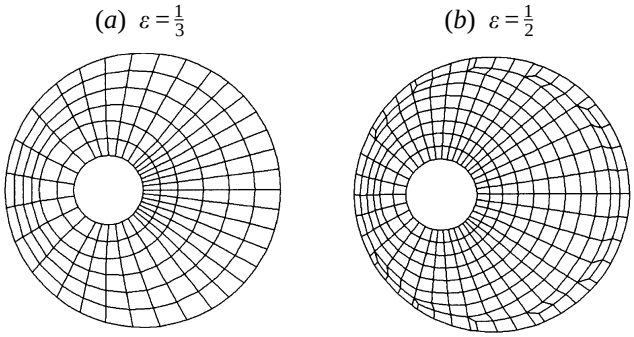

FIGURE 6. Eccentric cylinder analysis grids.

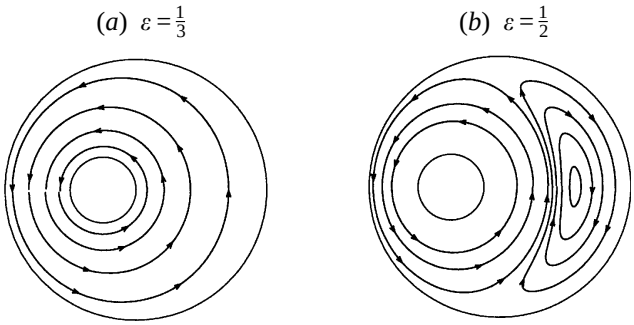

FIGURE 7. Pathlines from the FEM simulation of eccentric bearing problem for a Newtonian fluid for $Re = 0.09$.

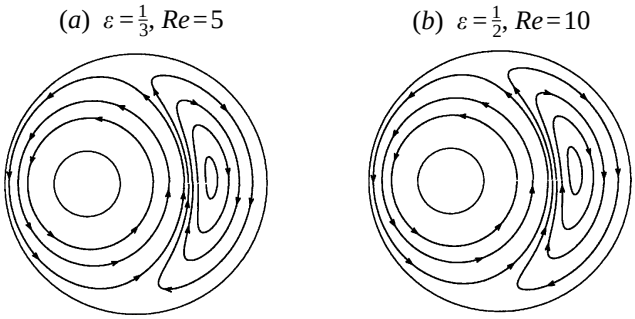

FIGURE 8. Pathlines from the FEM simulation of eccentric bearing problem for a Newtonian fluid.

5. Multidimensional particle migration

5.1. *Eccentric bearing experiments*

Unlike the case of the suspension flow in a concentric Couette device, no analytic solution is available for the steady-state particle distribution in a suspension flow between eccentric cylinders, so one must rely entirely upon numerical simulation and experiment. Phan-Thien *et al.* (1995) reported earlier experiments on an eccentric bearing test device with initial particle volume fraction of 0.50 in which NMR images of the particle distributions were obtained for $\varepsilon = \frac{1}{3}$ after 200, 800, and 14 000 revolutions of the inner cylinder. Also reported was the (supposed) steady-state distribution of solids for an eccentric bearing with $\varepsilon = \frac{1}{2}$. These NMR images

verified that shear-induced migration had indeed occurred in the eccentric bearing device. For $\varepsilon = \frac{1}{3}$, the particle distribution after 14 000 rotations of the inner cylinder is characterized by the formation of a particle depleted zone near the rotating cylinder, with the particle concentration increasing circumferentially in the direction of the stationary cylinder. The maximum particle concentration was observed over a large portion of the wide-gap region at the stationary cylinder. Similarly, for the case of $\varepsilon = \frac{1}{2}$, the solids distribution after 10 000 revolutions of the inner cylinder also contained a particle depleted zone near the rotating cylinder, and the particle concentration increased circumferentially toward the outer cylinder. The highest particle concentrations were confined to a crescent shaped portion of the wide-gap region, but now the maximum concentration occurred away from the outer cylinder. Additionally, the introduction of a tracer particle into the suspension flow indicated a region of very slow reverse flow in the wide-gap region.

The experiments described by Phan-Thien *et al.* (1995) were extended in the present study to obtain transient concentration profiles in the apparatus with $\varepsilon = \frac{1}{2}$. The suspensions were composed of polymethylmethacrylyate (PMMA) spherical particles with a mean diameter of 675 μm, suspended in a Newtonian liquid that was composed of a solution of three primary components: 50.27% by weight Triton x-100 (an alkylaryl polyether alcohol from J. T. Baker), 35.66% by weight H-90,000 UCON oil (a polyalkylene glycol made by Union Carbide), and 14.07% by weight practical grade 1,1,2,2 tetrabromoethane (TBE). A small amount (about 0.1% of the weight of TBE) of Tinuvin 328 (an antioxidant made by Ciba-Giegy) was dissolved in the TBE prior to mixing the solution to retard the breakdown of TBE when the solution is subjected to UV radiation. This solution was designed to have the same density as the PMMA particles at the room temperature of the NMR laboratory (approximately 22°C). The viscosity of the suspending liquid was 4.95 Pa s at this temperature. Again, the overall solids volume fraction of the suspension was 0.50.

The inner and outer cylinder radii were 0.64 cm and 2.54 cm, respectively. The inner cylinder was rotated at a rate of approximately 90 r.p.m. by a motor and halted after 40, 1000, 2000, 3000, 5000, and 10 000 revolutions so that NMR images could be taken. Because the particles were neutrally buoyant, no further movement of the particles occurred during the imaging sequence. Although the temperature of the suspension was controlled only by the ambient temperature of the laboratory, no settling or rising of the suspended particles was detected over the duration of the experiments. Moreover, no buoyancy-driven segregation was observed in NMR images of the suspension taken before and after the suspension was allowed to remain undisturbed overnight.

The NMR imaging techniques used in these experiments remained essentially the same as those described by Graham *et al.* (1991), but new hardware upgrades now allowed the creation of images in shorter times (static images were performed in 4 minutes). The imager (NALORAC Quest 4400) was interfaced with a 1.9 T, 31 cm horizontal bore magnet (Oxford) and controlling hardware. Experiments were controlled by a computer and a flexible state-device (MSC). Magnetic field gradients in the horizontal (X), vertical (Y), and axial (Z) directions were produced by currents flowing in a gradient coil assembly; these gradients were used to encode spatial information in the NMR signal. R.f. magnetic field pulses were applied through the transmit/receive switch to the r.f. probe which also received the NMR signal. The signal was heterodyned in phase quadrature to produce audio frequency signals which were then digitized and stored for processing.

NMR images were taken of a 2.4 cm thick cross-sectional (X, Y) slice of the

eccentric bearing apparatus, perpendicular to the outer cylinder axis, and about midway along its length in the axial direction. The fluid in this slice gave a full-intensity signal and the particles gave no signal. The normalized value of the image intensity was proportional to the density of the liquid-phase protons in a volume element. Initial experiments used an external calibration to determine the absolute value of the intensity signal corresponding to the suspending liquid. NMR images taken near the ends of the apparatus showed no evidence of particle migration in the axial direction, thus in later experiments the fluid fraction was sometimes calibrated by matching the averaged intensity of the image for the initial state to the known fluid fraction.

The in-plane spatial resolution of the image was approximately 0.2 mm. Typical signal to noise ratio (S/N) in the concentration images was 20. To distinguish small differences in concentration, several volume elements of the image must be averaged. The accuracy of NMRI measurements of fluid fraction, with the (S/N) ratio increased to 100 by averaging, is 1–3%, and the precision of the measurements is 3–5%.

Figure 9 shows the particle volume fraction across the midplane of the eccentric bearing with $\varepsilon = \frac{1}{3}$ for the images originally reported by Phan-Thien *et al.* (1995). Similarly, figures 10(*a*), 10(*b*), 10(*c*) and 10(*d*) show the particle volume fraction obtained from the image intensities along a horizontal line bisecting the inner rod of the apparatus after 40, 1000, 5000 and 10 000 turns for eccentricity $\varepsilon = \frac{1}{2}$. Note that the experimental values of figure 10(*d*) show an abrupt increase in particle concentration at about 1.75 cm from the centre. This may be an experimental artifact because the values reported here correspond to individual picture elements (pixels) along the horizontal. Thus these results contain more scatter than values reported for the concentric cylinder apparatus (figure 2) in which a number of pixel values at equal radius from the rotating cylinder are averaged circumferentially. Figure 11(*a*) shows NMR images taken in the bearing for $\varepsilon = \frac{1}{2}$ after 40, 1000, 2000, 3000, and 5000 revolutions of the inner cylinder. The false-colour images show that dramatic changes occur over time in the solids concentration. These NMR images contain quantitative information as explained above.

5.2. *Eccentric bearing simulations*

We consider numerically the same two problems in the eccentric bearing geometry as mentioned in the experiments described above. For both problems, the initial uniform particle concentration is given by $\phi = 0.50$, $R_o = 2.54$ cm, $R_i = 0.64$ cm, $K_c = 0.41$, and $K_\mu = 0.62$. For the first problem, the eccentricity ratio is $\varepsilon = \frac{1}{3}$, and for the second problem, $\varepsilon = \frac{1}{2}$.

The first problem, $\varepsilon = \frac{1}{3}$, was modelled using the grid shown in figure 6(*a*) resulting in a discretization having 2740 degrees of freedom. The particle concentration profiles from this analysis are included in figure 9. The numerical results after 1500 turns are seen to be in reasonable agreement with the experimental results recorded after 14 000 turns. The difference between the numerical results after 1050 turns and 1500 turns indicates that the numerical solutions are nearly converged to the steady state. As expected, no region of recirculation is observed in the simulation. Phan-Thien *et al.* (1995) and Fang & Phan-Thien (1995) analysed this problem using a finite volume method and the current FEM results are consistent with their analysis.

The second probem with $\varepsilon = \frac{1}{2}$ was numerically analysed using the grid shown in figure 6(*b*) which resulted in 4201 degrees of freedom. Results obtained from the numerical analysis are compared with the experimental results in figure 10, which

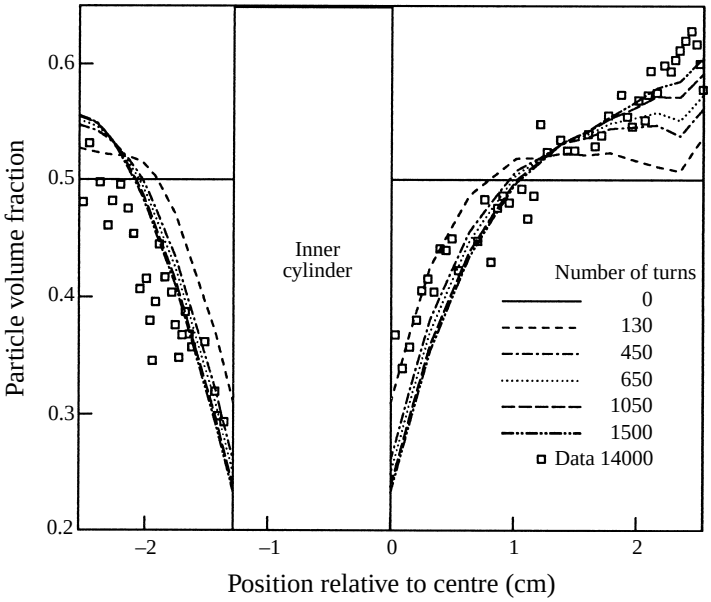

FIGURE 9. Particle volume fraction along the horizontal midplane of the eccentric bearing for $\varepsilon = \frac{1}{3}$ and various numbers of turns of the inner cylinder.

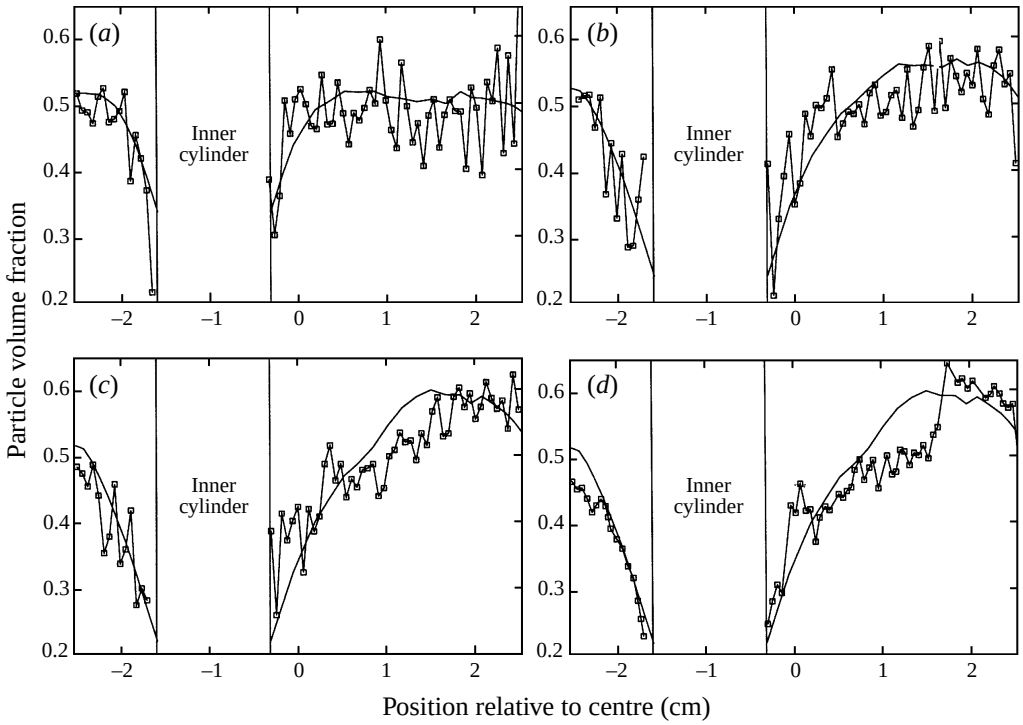

FIGURE 10. Computed and experimental (□) particle volume fraction along the horizontal midplane of the eccentric bearing for $\varepsilon = \frac{1}{2}$ and (*a*) 40, (*b*) 1000, (*c*) 5000 and (*d*) 6000 (computed) and 10 000 (experimental) turns of the inner cylinder.

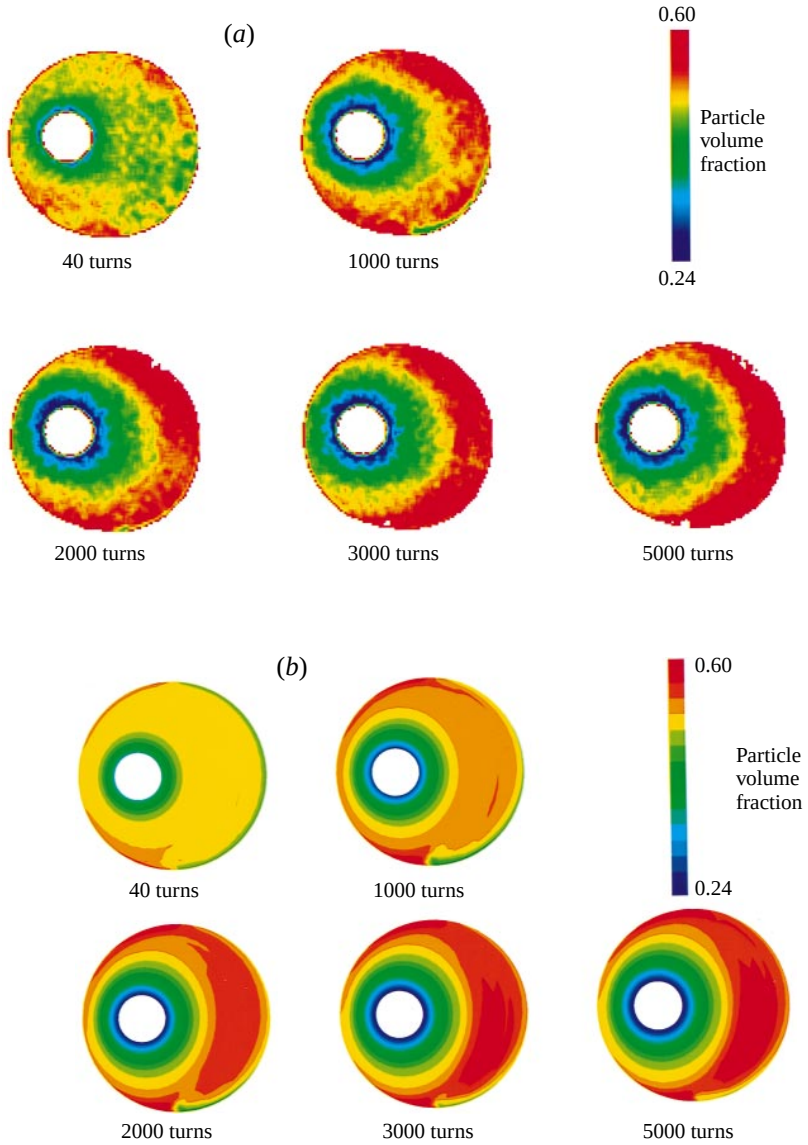

FIGURE 11. (*a*) NMR images and (*b*) numerical predictions of solids distribution after various numbers of revolutions of the inner cylinder in the apparatus with $\varepsilon = \frac{1}{2}$.

displays the particle volume fraction distribution along the horizontal diameter of symmetry. Again, there is relatively good agreement between the numerical and the experimental results. The plot of computed particle volume fraction along the horizontal for 6000 turns (figure 10*d*) indicates that the local maximum concentration occurs away from the outer cylinder and is consistent with the experimental steady-state measurement.

The numerically predicted series of transient concentration profiles corresponding to the present experimental results is shown in figure 11(*b*). General qualitative agreement between the computed and experimental results indicates that the current FEM analysis with the diffusive flux constitutive model for the concentration is

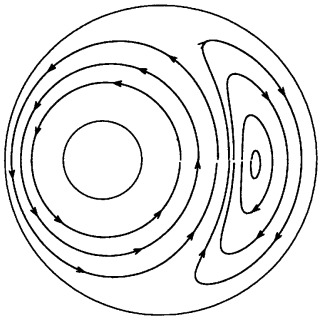

FIGURE 12. Particle pathlines from FEM simulation of the eccentric bearing for $\varepsilon = \frac{1}{2}$ and 6000 turns of the inner cylinder.

capable of following the evolution of the non-uniform concentration profile through the transient stages. As in the case of $\varepsilon = \frac{1}{3}$, there is a general migration of the particles away from the inner cylinder towards the outer cylinder and a large region of concentrated particle phase forms in the wide gap. However, in contrast to the case of $\varepsilon = \frac{1}{3}$, the maximum concentration in the bearing occurs not along the horizontal of geometric symmetry, but at the outer cylinder in a small region along the lower edge of the bearing. Additionally, the transition toward steady state is not as uniform and the near symmetry that was evident in the concentration profiles for the case $\varepsilon = \frac{1}{3}$ no longer exists for $\varepsilon = \frac{1}{2}$, either numerically or experimentally.

Flow pathlines for the $\varepsilon = \frac{1}{2}$ case after 6000 rotations of the inner cylinder calculated from the numerical results, figure 12, verify the presence of two distinct flow regimes. These two distinct flow regimes within the eccentric bearing must be accompanied by a dividing streamline which denotes a demarcation between the two flow regions. The pathlines demonstrate the asymmetry of the flow about the horizontal axis, as there is a slight shift of the recirculation flow centre in a direction opposite to the inner cylinder rotation. Like the suspension flow, the particle concentration distribution in the eccentric bearing also contains two distinct distributions which correspond loosely to the two flow regions, one in the primary flow region and one in the wide gap.

Phan-Thien *et al.* (1995) modelled the eccentric bearing problem for $\varepsilon = \frac{1}{2}$ using a finite volume method and an unstructured grid. In these simulations they were unable to observe the recirculating flow in the wide gap. Furthermore, the model predicted that the highest values of concentration occurred along the stationary cylinder in the wide-gap portion of the bearing. Fang & Phan-Thien (1995) later modelled the same problem using a finite volume method employing a structured grid. In their simulations, they were able to observe the recirculation region at a lower initial particle volume fraction (0.20). However, owing to numerical instabilities, they were unable to obtain steady solutions for a particle volume fraction of 0.50.

Further study of the computed results provides additional insight into the structure of the particle concentration distribution. In particular, we consider the magnitude of velocity in the wide-gap region along a horizontal line directed from the centre of the inner cylinder to the outer cylinder. In the case of $\varepsilon = \frac{1}{3}$, the suspension velocity is perpendicular to this horizontal line. Additionally, both the magnitude of velocity and the corresponding value of velocity gradient decrease monotonically moving away from the inner cylinder. A plot of generalized shear for this flow (figure 13*a*) demonstrates the correspondence between low values of generalized shear and higher particle concentrations (see figure 9).

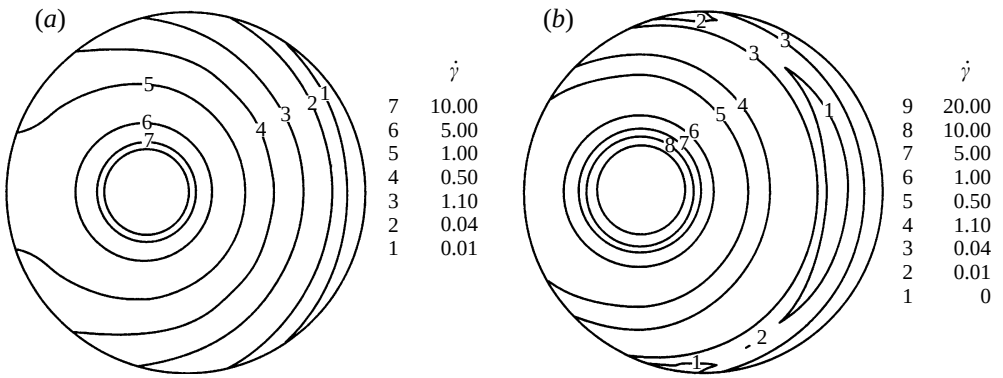

FIGURE 13. Generalized shear rate from FEM simulation of the eccentric bearing for (*a*) $\varepsilon = \frac{1}{3}$ and 1500 turns of the inner cylinder, and (*b*) $\epsilon = \frac{1}{2}$ and 6000 turns of the inner cylinder.

Similarly, for the case of $\varepsilon = \frac{1}{2}$, we consider the magnitude of velocity in the wide-gap region along a line directed from the centre of the inner cylinder toward the centre of the recirculation zone, where the suspension velocity is nearly perpendicular to this line. Moving toward the right, away from the inner cylinder into the gap region, the velocity field remains continuous across the dividing streamline, decreasing from its maximum value at the inner cylinder to zero at the centre of the recirculation zone. Thus the corresponding component of velocity gradient also decreases in magnitude along this line segment. Proceeding along the same line beyond the centre of the recirculation zone, the velocity reverses direction and the magnitude of velocity increases slightly before finally diminishing in magnitude to satisfy the no-slip condition at the outer cylinder. The corresponding magnitude of velocity gradient first decreases to zero and then increases to a finite value at the wall. Over nearly half of the recirculation zone, this same basic character is repeated along radial lines extending from the inner cylinder and terminating at the outer cylinder. These trends in the velocity gradient lead to the presence of a narrow region in which the second invariant of shear rate, and thus the generalized shear rate, is a local minimum as shown in figure 13(*b*). This view is also supported by the numerical results in figure 11(*b*) since the particle concentration continues to increase where the generalized shear rate is low.

It is interesting to note some of the fine-scale features that are present in both the numerical analysis and experiment (figures 11(*a*) and 11(*b*)). Before 2000 turns of the inner cylinder, a small region of high concentration can be observed at the stationary wall beneath the rotating cylinder in both the computed results and in the experiment. The FEM results also include a small region of high concentration above the rotating cylinder, but the small high-concentration region beneath the cylinder seems to extend further from the outer wall than the one above the cylinder. The velocity within the recirculation region is generally lower than the velocity in the primary flow on the opposite side of the dividing streamline. However, near the intersection of the dividing streamline and the outer cylinder, the two velocities are more closely matched, thus approaching conditions similar to those present along the centreline of a Poiseuille flow. That is, the generalized shear rate, $\dot{\gamma}$, is nearly zero and attains a local minimum in this region resulting in a high particle concentration.

The developing concentration profiles do not exhibit symmetry about the horizontal centreline of the eccentric cylinder (figures 11(*a*) and 11(*b*)). The primary flow about

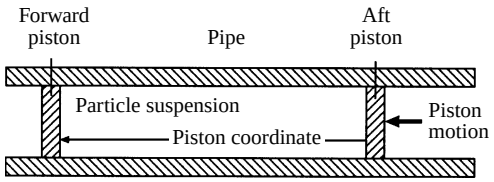

FIGURE 14. Schematic of piston-driven flow.

the right-hand portion of the inner cylinder is an expansion flow beneath the cylinder and a contraction flow above the cylinder. Thus in one case convected particles are decelerating and in the other case convected particles are accelerating. The fact that convected particles are decelerating as they approach the dividing streamline at the lower portion of the outer cylinder could partially explain the local increase in particle volume fraction. Similarly, because convected particles at the upper portion of the bearing are accelerating one should not expect the same local increase as in the lower portion of the bearing. Because the velocity distributions develop much more quickly than the concentration profiles it also follows that the initial development of these small regions of high concentration is largely influenced by particle convection while shear-induced particle migration becomes more noticeable much later.

One additional feature appearing in both experiment and the numerical predictions cannot be overlooked. At about 1000 turns of the inner cylinder, a thin region (green) of lower concentration forms along the outer wall directly beyond the small high-concentration region. This feature is visible in both the experimental and numerical profiles up to 2000 turns, but later diminishes as the suspension concentration profile in the wide gap approaches a more steady configuration.

5.3. *Piston-driven flow experiments*

A common method of displacing a fixed volume of suspension is to mechanically move it down a pipe by means of a piston. This technique is most likely to be used in batch processing where the exiting suspension often forms a free surface. In applications such as injection moulding of a composite material, the quality of the finished product may rely heavily upon the uniformity of the suspension downstream of the piston. As a prelude to studying the more complex free surface supension transport problem, we considered the displacement of a suspension between two pistons as shown in figure 14.

Two identical pistons, sealed with O-rings, slid within a pipe of inner radius 2.54 cm. Depending upon the the type of NMR image desired, two different but equivalent means of driving the suspension flow were employed: displacement of the piston or displacement of the pipe. Displacement motion was accomplished using a long push rod connected to a motor-driven 45 cm long screw located across the room (thereby eliminating any possible mechanical or electromagnetic interference between the imaging magnet and the motor). In cases where a particular section of the suspension was to be kept in the imaging volume of the magnet, the aft piston was held stationary and the pipe was translated at a constant velocity. Otherwise, the push rod moved the aft piston at a constant velocity of 0.0625 cm s^{-1} while the pipe was held stationary. In both cases, the forward piston was always free.

The suspending liquid was the same as described in §5.1. Different sizes of suspended PMMA particles were used in each experiment, sieved spheres with an average diameter of 678 μm or uniform, ground spheres with a diameter of 3178 μm. Both suspensions had an overall volume fraction of solids of 0.50.

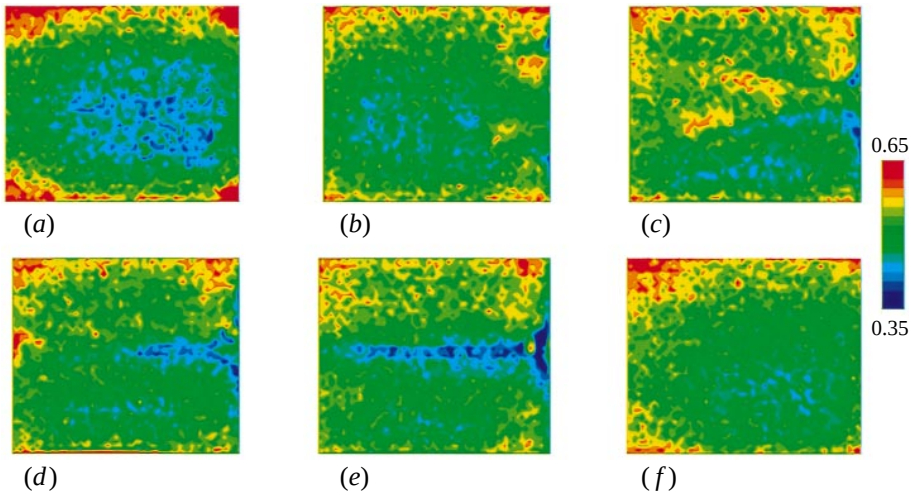

FIGURE 15. NMR images of suspension particle volume fraction adjacent to the aft piston (right-side) of (*a*) initial state, and (*b*) after piston travel of 2 diameters, (*c*) 3 diameters, (*d*) 4 diameters, (*e*) 5 diameters; and (*f*) the forward piston (left-hand side) in piston-driven flow after 5 diameters of piston travel.

Initially, the forward piston was inserted in the pipe, then 30 cm of the pipe was filled with suspension, and the suspension in the pipe was remixed. After allowing the suspension to de-gas, the apparatus was then sealed with the aft piston. The entire apparatus was placed coaxially in the magnet and initial NMR images were taken along the length of the apparatus before the motor was activated. The averaged intensity of the images depicting the initial state was normalized to the known average concentration of the suspension. The motor-driven push rod was then allowed to displace either the aft piston (with the pipe wall held stationary) or the pipe wall (with the aft piston held stationary). For low rates of displacement, inertial forces were insignificant, and since the particles were neutrally buoyant in the liquid, fluid suspension motion ceased when the motor stopped. This permitted static images to be recorded whenever the motor was stopped.

During the experiment, regions of suspension near the pistons were imaged in a 0.5 mm thick vertical slice along the pipe axis. Processed NMR images of the region near the aft piston for the suspension containing 678 μm diameter particles are shown in figure 15 for the initial state and after a piston travel of 2, 3, 4, and 5 pipe diameters. These images indicate the development of a 'spike' of liquid-rich suspension forming along the pipe axis near the aft piston. This at first seemed surprising because in "pressure-driven" pipe flow the particles migrate toward the centreline thus forming a liquid-depleted region near the pipe axis. In contrast to the region near the aft piston, the imaged region near the forward piston, figure 15(*f*), showed no features strong enough to be detected with the NMR technique, even after 5 pipe diameters of piston travel.

Additional information concerning particle migration was obtained by scanning the entire length of suspension-filled pipe to obtain a measurement of the cross-sectional area-averaged liquid volume fraction as a function of the axial distance along the pipe and the distance of travel. Figure 16(*a*) indicates that after 5 pipe diameters of travel, there is a slight accumulation of particles near the forward piston. Note

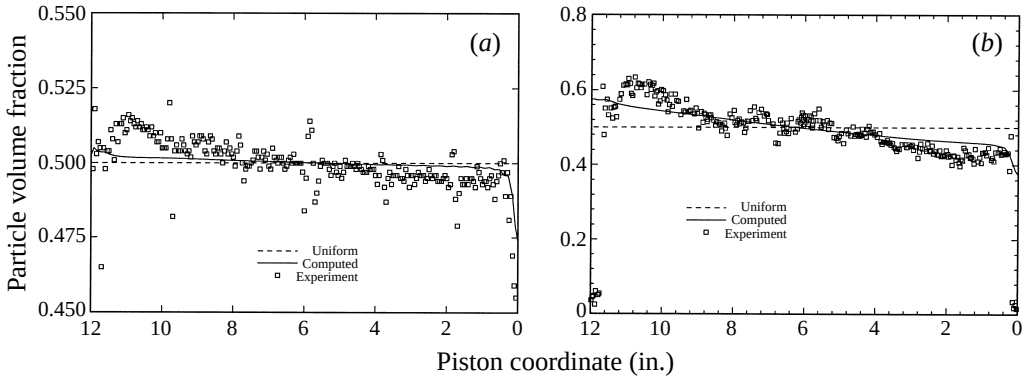

FIGURE 16. Piston flow, area-averaged axial particle volume fraction for (*a*) 678 μm particles and (*b*) 3178 μm particles.

that due to limitations in the experimental apparatus, these profiles are not near the steady state.

Similar experiments were also performed using a supension with the larger 3178 μm diameter particles. It is worth noting that due to the size of these particles, it is only possible to place a maximum of 16 particles across the diameter of the pipe. For the suspension of larger particles, the liquid-rich spike near the aft piston was not observed in the NMR images. It is quite possible that this spike could not be observed because the particles were so large compared to the length scales of the apparatus. However, axial migration could again clearly be detected, as shown in the plot of section-averaged liquid volume fraction versus axial position along the pipe, figure 16(*b*).

5.4. *Piston-driven flow simulations*

An axisymmetric model of the piston and pipe geometry was constructed using a grid which resulted in 3168 degrees of freedom. The problem was modelled in much the same way as a shear-driven cavity flow where an axial velocity boundary condition is applied to the closed piston system at the pipe wall. That is, rather than having the pistons move through a stationary length of pipe, the pistons are held stationary and the walls move at a constant velocity as described in the experimental procedures. The empirical constants K_c and K_μ in the model were the same as in the previous problems. A transient analysis using the NACHOS II FEM code was performed of the piston flow problem for both sizes of particles used in the experiments described above. Whereas the experiments were only carried out for a total travel of 5 pipe diameters, these simulations were carried out for a total piston travel of 15 pipe diameters.

The numerical results indicate that the velocity field becomes essentially fully developed within one piston diameter of travel. Plots of the developed velocity field and streamlines shown in figure 17 demonstrate that the suspension motion is essentially a recirculating flow with the flow along the pipe wall moving in one direction and the flow near the centreline axis moving in the opposite direction. As the suspension near the wall approaches the aft piston, its velocity first decreases and then reverses direction, thus forming a localized region of low velocity and low shear near the centre of the piston. Similarly, as the suspension along the centreline axis approaches the forward piston its velocity also decreases and then reverses direction,

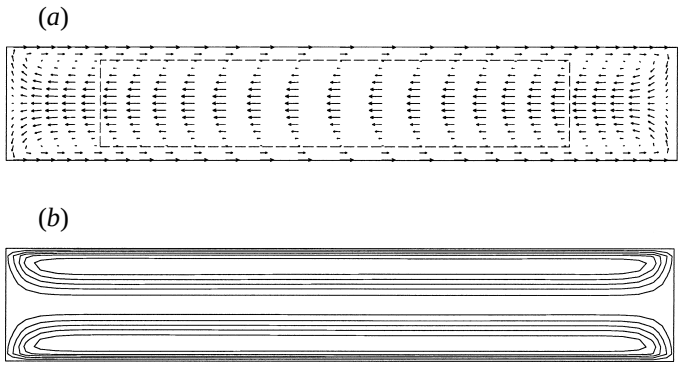

FIGURE 17. (*a*) Suspension velocity field and (*b*) streamlines.

thus forming another localised region of low velocity and low shear near the centre of the piston.

A series of plots showing the predicted particle concentration profile development is shown in figure 18(*a*) for the 678 μm spheres and in figure 18(*b*) for the 3178 μm spheres, respectively, after piston travels of 5, 10, and 15 pipe diameters. In the light of the above observations of regions of low shear rate near both pistons, these concentration predictions are somewhat puzzling since one might expect the particle concentration to increase at both pistons, and not only at the leading piston. This result can be explained by considering the core region in the flow shown by the dashed box in the velocity field plot (figure 17). From this figure, we note that the flow profile in this region is much like that in the pipe flow. Since we know that suspension flows in pipes contain regions of low shear along the pipe centreline, particles tend to migrate towards the pipe axis. Assuming that locally the particle and fluid velocity are roughly equal, the average particle velocity will then be larger than the average fluid velocity since the particles are concentrated in the high-velocity region in the centre of the pipe. Hence, particles will tend to be convected towards the front piston and away from the back piston as indicated in figure 16, where one sees that the concentration increases monotonically moving from the aft piston toward the forward piston. These figures indicate that the simulations predict the same trends as the experiments. However, the experimental results in this transient region indicate that particle migration occurs faster than predicted by the diffusive flux model.

In some portion of the flow domain away from the pistons, the development length of the concentration profile can be approximated with the scaling arguments of Nott & Brady (1994) given by (4.6). According to this scaling, full development of the radial concentration profile can be expected at a distance L for $(L/R_o) > (R_o/a)^2$ where R_o is the piston radius so that $(R_o/a)^2 \sim 5614$ for the 678 μm spheres and $(R_o/a)^2 \sim 256$ for the 3178 μm spheres. Setting $L = 30$ cm as the distance between the forward and aft pistons then $(L/R_o) \sim 11.8$. Thus even allowing for a multiplicative factor of two or three discrepancy in the overall scaling, (L/R_o) does not exceed $(R_o/a)^2$ and full development of the radial profile should not be expected for the aspect ratio of our experimental geometry.

Overall, there is reasonable agreement between the numerical and experimental results. Similar features are seen in both sets of calculated results, namely an axial gradient in liquid concentrations and higher liquid concentration along the pipe axis near the aft piston for the suspension of smaller particles. The predicted region of high

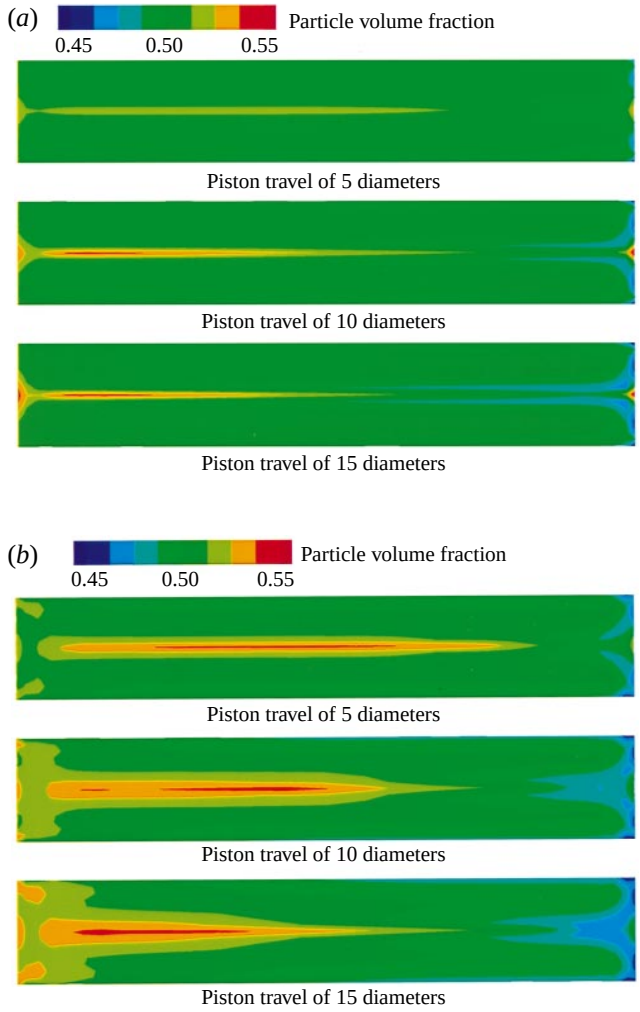

FIGURE 18. FEM predictions of particle concentration profiles resulting from piston-driven flow for a suspension of (*a*) 678 μm diameter and (*b*) 3178 μm diameter spheres with an overall particle volume fraction of 0.50.

particle content near the pipe axis in the vicinity of the forward piston is not observed experimentally, however. In the case of smaller particles, it must be noted that the changes in concentration are relatively small and the limits of the NMR imaging technique may be a factor in the discrepancy between simulation and experiment.

Although the numerical simulations can be performed for particle suspensions containing particles of any size, there are obvious limits to the applicability of the present FEM formulation. In the case of piston flow with 3178 μm particles, the particles are large compared with the flow area so that the suspension motion may depend more upon individual particle motions than upon the averaged motion of groups of particles, thus the continuum assumption becomes questionable. This would be particularly true near the pistons where the suspension flow must change direction and could partially explain the absence of fine detail in the experimental radial particle concentration distribution. Nevertheless, the overall axial structure of particle concentration distribution, transition from a concentrated region of particles near

the front piston to a depleted particle region near the back piston, predicted by the simulation is also observed experimentally.

6. Conclusions

We have shown the ability to simulate the complex behaviour of suspensions containing neutrally-buoyant spheres in a Newtonian liquid using a Galerkin, finite element, Navier–Stokes solver. A continuum diffusive flux model described by Phillips *et al.* (1992) has been incorporated into the finite element formulation. This model couples a Newtonian stress/shear-rate relationship with a shear-induced migration model of the suspended particles in which the local effective viscosity is dependent on the local volume fraction of solids. The model, which originally described particle migration in terms of a shear rate is, for multidimensional flows, now couched in terms of the second invariant of the generalized shear rate. The shear-induced migration model is shown here to be surprisingly robust at capturing the essential features in two-dimensional and three-dimensional (axisymmetric) suspension flows, such as flow in a journal bearing and piston-driven flow in a pipe. However, the equations are very stiff and previous failures to accurately predict journal bearing flows of highly concentrated suspensions using this same constitutive formulation in finite volume based codes argue for caution in its use.

To provide experimental data with which to benchmark our finite element code, we have used nuclear magnetic resonance imaging to non-invasively determine the evolution of the solids-concentration profiles of initially well-mixed suspensions subjected to slow flow. Multidimensional flows of suspensions result in complex final distribution of the solids, causing rheological behaviour that cannot be accurately described with typical single-phase constitutive equations. For example, in the flow between eccentric cylinders, the location of the region of highest concentration depends strongly on the eccentricity ratio. With piston-driven flow in a pipe, the particle concentration evolves both axially and radially. Symmetry expected in Newtonian flows disappears due to these concentration changes. Furthermore, especially at higher concentrations, gradients in concentration can cause much more severe gradients in effective viscosity.

Given that the current computed results are most often consistent with both previous results and with experiments, it seems reasonable to expect continued advances in numerical modelling of suspension flows. Efforts should be directed at determining the limits of this type of continuum modelling when applied to flows of discrete multiphase systems. For example, an improved model would include some degree of anisotropy that is typically present in suspensions.

The authors would like to thank Dr David Gartling of Sandia National Laboratories for many thoughtful discussions and useful advice. This work was sponsored by the US Department of Energy, at Sandia National Laboratories under Contract DE-AL04-94AL85000, and at Los Alamos National Laboratory under Contract W-7405-ENG-36 with the University of California. The authors gratefully acknowledge partial support of this work through the US Department of Energy, Division of Engineering and Geosciences, Office of Basic Energy Sciences, and the Mechanics and Energy Conversion Division, Office of Naval Research. Partial support was also provided by the US Department of Energy Applied Mathematical Sciences Division Grand Challenge Applications Program. Additionally, partial support was provided to the Lovelace Institutes by the US Department of Energy, Pittsburg Energy Technology Center via grant DE-FG22-94PC94248.

REFERENCES

Abbott, J. R., Tetlow, N., Graham, A. L., Altobelli, S. A., Fukushima, E., Mondy, L. A. & Stephens, T. A. 1991 Experimental observations of particle migration in concentrated suspensions: Couette flow. *J. Rheol.* **35**, 773–794.

Arp, P. A. & Mason, S. G. 1977 The Kinetics of Flowing Dispersions IX. Doublets of Rigid Spheres (Experimental). *J. Colloid Interface Sci.* **61**, 44–61.

Ballal, B. Y. & Rivlin, R. S. 1976 Flow of a Newtonian fluid between eccentric rotating cylinders. *Arch. Rat. Mech. Anal.* **62**, 237–294.

Baree, R. D. & Conway, M. W. 1994 Experimental and numerical modeling of convective proppant transport. *Soc. Petrol. Engrs* SPE 28564.

Brady, J. F. & Bossis, G. 1988 Stokesian Dynamics. *Ann. Rev. Fluid Mech.* **20**, 111–157.

Chapman, B. K. 1990 Shear induced migration in concentrated suspensions. PhD Thesis, University of Notre Dame.

Chow, A. W., Sinton, S. W., Iwamiya, J. H. & Stephens, T. S. 1994 Shear-induced migration in Couette and parallel-plate viscometers: NMR imaging and stress measurements. *Phys. Fluids* A **6**, 2561–2576.

Clifton, R. J., Brown, U. & Wang, J.-J. 1988 Multiple fluids, proppant transport, and thermal effects in three-dimensional simulation of hydraulic fracturing. *Soc. Petrol Engrs* SPE 18198.

DiPrima, R. C. & Stuart, J. T. 1972 Flow between eccentric rotating cylinders. *J. Fluid Lubr. Tech.* **94**, 266–274.

Fang, Z. & Phan-Thien, N. 1995 Numerical simulation of particle migration in concentrated suspensions by a finite volume method. *J. Non-Newtonian Fluid Mech.* **58**, 67–81.

Gartling, D. K. 1986 NACHOS II-A Finite Element Computer Program For Incompressible Flow Problems. Tech. Rep. SAND86-1817 Sandia National Laboratories, Albuquerque, NM, USA.

Gartling, D. K. & Reddy, J. N 1994 *The Finite Element Method in Heat Transfer and Fluid Dynamics.* CRC.

Givler, R. C., Crochet, M. J. & Pipes, R. B. 1983 Numerical predictions of fiber orientation in dilute suspensions. *J. Compos. Mater.* **17**, 330–343.

Graham, A. L., Altobelli, S. A., Fukushima, E., Mondy, L. A. & Stephens, T. S. 1991 Note: NMR imaging of shear-induced diffusion and structure in concentrated suspensions undergoing Couette flow. *J. Rheol.* **35**, 191–201.

Hampton, R. E. 1996 An investigation of migration of particles in pressure-driven flow in a circular conduit. MS Thesis, University of Washington.

Hampton, R. E., Mammoli, A. A., Graham, A. L., Tetlow, N. & Altobelli, S. A. 1997 Migration of particles undergoing pressure-driven flow in a circular conduit. *J. Rheol.* **41**, 621–640.

Husband, D. M. 1989 Continuous processing of composite solid propellants. *Chem. Engng Prog.* **85**, 55–61.

Ingber, M. S. 1989 Dynamic simulation of the hydrodynamic interaction among immersed particles in Stokes flow. *Intl J. Numer. Meth. Fluids* **9**, 263–273.

Jana, S. C., Kapoor, B. & Acrivos, A. 1995 Apparent wall slip velocity coefficients in concentrated suspensions of noncolloidal particles. *J. Rheol.* **39**, 1123–1132.

Jenkins, J. T. & McTigue, D. M. 1990 Transport processes in concentrated suspensions: The role of particle fluctuations. In *Two-Phase Flows and Waves* (ed. D. D. Joseph & D. G. Schaffer), pp. 70–79. Springer.

Kamal, M. M. 1966 Separation in the flow between eccentric rotating cylinders. *Trans. ASME J. Basic Engng* **88**, 717–724.

Karilla, S. J., Fuentes, Y. O. & Kim, S. 1989 Parallel computational strategies for hydrodynamic interactions between rigid particles of arbitrary shape in a viscous fluid. *J. Rheol.* **33**, 913–947.

Karnis, A., Goldsmith, H. L. & Mason, S. G. 1966 The kinetics of flowing dispersions I. Concentrated suspensions of rigid particles. *J. Colloid Interface Sci.* **22**, 531–553.

Kelmanson, M. A. 1984 A boundary integral equation method for the study of slow flow in bearings with arbitrary geometries. *J. Tribol.* **106**, 260–264.

Koh, C. J., Hookham, P. & Leal, L. G. 1994 An experimental investigation of concentrated suspension flows in a rectangular channel. *J. Fluid Mech.* **266**, 1–32.

Krieger, I. M. 1972 Rheology of monodisperse latices. *Adv. Colloid Interface Sci.* **3**, 111–136.

Krishnan, G. P., Beimfohr, S. & Leighton, D. T. 1996 Shear-induced radial segregation in bidisperse suspensions. *J. Fluid Mech.* **321**, 371–393.

Lee, R. L., Gresho, P. M. & Sani, R. L. 1979 Smoothing techinques for certain primitive variable solutions of the Navier–Stokes equations. *Intl J. Numer. Methods Engng* **14**, 1785–1804.

Leighton, D. & Acrivos, A. 1986 Viscous resuspension *Chem. Engng Sci.* **41**, 1377–1384.

Leighton, D. & Acrivos, A. 1987*a* Measurement of shear-induced self-diffusion in concentrated suspensions of spheres. *J. Fluid Mech.* **177**, 109–131.

Leighton, D. & Acrivos, A. 1987*b* The shear-induced migration of particles in concentrated suspensions. *J. Fluid Mech.* **181**, 415–439.

Mills, P. & Snabre, P. 1995 Rheology and structure of concentrated suspensions of hard spheres. Shear induced particle migration *J. Phys. Paris II* **2**, 1597–1608.

Mondy, L. A., Brenner, H., Altobelli, S. A., Abbott, J. R. & Graham, A. L. 1994 Shear-induced particle migration in suspensions of rods. *J. Rheol.* **38**, 444–452.

Nott, P. R. & Brady, J. F. 1994 Pressure-driven flow of suspensions: simulation and theory *J. Fluid Mech.* **275**, 157–199.

Phan-Thien, N. & Fang, Z. 1996 Entrance length and pulsatile flows of a model concentrated suspension. *J. Rheol.* **40**, 521–529.

Phan-Thien, N., Graham, A. L., Altobelli, S. A., Abbott, J. R. & Mondy, L. A. 1995 Hydrodynamic particle migration in a concentrated suspension undergoing flow between rotating eccentric cylinders. *Ind. Engng Chem. Res.* **34**, 3187–3194.

Phillips, R. J., Armstrong, R. C., Brown, R. A., Graham, A. L. & Abbott J. R. 1992 A constitutive equation for concentrated suspensions that accounts for shear-induced particle migration. *Phys. Fluids* A **4**, 30–40.

San Andres, A. & Szeri, A. Z. 1984 Flow between eccentric rotating cylinders. *J. Appl. Mech.* **51**, 869–878.

Sood, D. R. & Elrod, H. G. 1970 *Rep. 17*. Lub. Res. Lab.Columbia University, NY USA, pp. 1–44.

Tetlow, N., Graham, A. L., Ingber, M. S., Subia, S. R., Mondy, L. A. & Altobelli, S. A. 1998 Particle migration in a Couette apparatus: Experiment and modeling. *J. Rheol.* **42**, 307–327.

Tran-Cong, T. & Phan-Thien, N. 1989 Stokes problems of multiparticle systems: a numerical method for arbitrary flows. *Phys. Fluids* A **1**, 453–461.

Unwin, A. T. & Hammond, P. S. 1990 Computer simulations of proppant transport in a hydraulic fracture. *Soc. Petrol. Engrs* SPE 29649.

Wannier, G. H. 1950 A contribution to the hydrodynamics of lubrication. *Q. Appl. Maths*, 1–32.

Zhang, K. & Acrivos, A. 1994 Viscous resuspension in fully developed laminar pipe flows. *Intl. J. Multiphase Flow* **20**, 579–591.

Zienkiewicz, O. C. 1967 *The Finite Element Method*. McGraw-Hill.